UCLA
UCLA Previously Published Works

Title
Wave Phenomena and Beam-Plasma Interactions at the Magnetopause Reconnection Region

Permalink
https://escholarship.org/uc/item/2j6846zb

Journal
Journal of Geophysical Research Space Physics, 123(2)

ISSN
2169-9380

Authors
Burch, JL
Webster, JM
Genestreti, KJ
et al.

Publication Date
2018-02-01

DOI
10.1002/2017ja024789

Peer reviewed

eScholarship.org Powered by the California Digital Library
University of California

AGU PUBLICATIONS

JGR

Journal of Geophysical Research: Space Physics

RESEARCH ARTICLE
10.1002/2017JA024789

Special Section:
Magnetospheric Multiscale (MMS) mission results throughout the first primary mission phase

Wave Phenomena and Beam-Plasma Interactions at the Magnetopause Reconnection Region

J. L. Burch[1], J. M. Webster[2], K. J. Genestreti[3], R. B. Torbert[1,4], B. L. Giles[5], S. A. Fuselier[1], J. C. Dorelli[5], A. C. Rager[5,6], T. D. Phan[7], R. C. Allen[8], L.-J. Chen[9], S. Wang[9], O. Le Contel[10], C. T. Russell[11], R. J. Strangeway[11], R. E. Ergun[12], A. N. Jaynes[13], P.-A. Lindqvist[14], D. B. Graham[15], F. D. Wilder[12], K.-J. Hwang[1], and J. Goldstein[1]

[1]Southwest Research Institute, San Antonio, TX, USA, [2]Department of Physics and Astronomy, Rice University, Houston, TX, USA, [3]Space Research Institute, Austrian Academy of Sciences, Graz, Austria, [4]Department of Physics, University of New Hampshire, Durham, NH, USA, [5]NASA, Goddard Space Flight Center, Greenbelt, MD, USA, [6]Department of Physics, Catholic University of America, Washington, DC, USA, [7]Space Sciences Laboratory, University of California, Berkeley, CA, USA, [8]Applied Physics Laboratory, The Johns Hopkins University, Laurel, MD, USA, [9]Department of Astronomy, University of Maryland, College Park, MD, USA, [10]Laboratoire de Physique des Plasmas, CNRS, Ecole Polytechnique, UPMC University Paris 06, Université Paris-Sud, Observatoire de Paris, Paris, France, [11]Earth and Planetary Sciences, University of California, Los Angeles, CA, USA, [12]LASP, University of Colorado Boulder, Boulder, CO, USA, [13]Department of Physics and Astronomy, University of Iowa, Iowa City, IA, USA, [14]Royal Institute of Technology, Stockholm, Sweden, [15]Swedish Institute of Space Physics, Uppsala, Sweden

Key Points:
- Whistler mode chorus and higher-frequency electrostatic waves were observed in the vicinity of a reconnection diffusion region at the dayside magnetopause
- The location of the Earthward boundary of chorus and electrostatic waves coincides with the opening of magnetic field lines via reconnection
- The causes of whistler mode chorus and electrostatic waves are shown to be electron temperature anisotropy and beam-plasma interactions, respectively

Correspondence to:
J. L. Burch,
jburch@swri.edu

Citation:
Burch, J. L., Webster, J. M., Genestreti, K. J., Torbert, R. B., Giles, B. L., Fuselier, S. A., … Goldstein, J. (2018). Wave phenomena and beam-plasma interactions at the magnetopause reconnection region. *Journal of Geophysical Research: Space Physics*, *123*, 1118–1133. https://doi.org/10.1002/2017JA024789

Received 22 SEP 2017
Accepted 10 JAN 2018
Accepted article online 19 JAN 2018
Published online 3 FEB 2018

©2018. The Authors.
This is an open access article under the terms of the Creative Commons Attribution-NonCommercial-NoDerivs License, which permits use and distribution in any medium, provided the original work is properly cited, the use is non-commercial and no modifications or adaptations are made.

Abstract This paper reports on Magnetospheric Multiscale observations of whistler mode chorus and higher-frequency electrostatic waves near and within a reconnection diffusion region on 23 November 2016. The diffusion region is bounded by crescent-shaped electron distributions and associated dissipation just upstream of the X-line and by magnetic field-aligned currents and electric fields leading to dissipation near the electron stagnation point. Measurements were made southward of the X-line as determined by southward directed ion and electron jets. We show that electrostatic wave generation is due to magnetosheath electron beams formed by the electron jets as they interact with a cold background plasma and more energetic population of magnetospheric electrons. On the magnetosphere side of the X-line the electron beams are accompanied by a strong perpendicular electron temperature anisotropy, which is shown to be the source of an observed rising-tone whistler mode chorus event. We show that the apex of the chorus event and the onset of electrostatic waves coincide with the opening of magnetic field lines at the electron stagnation point.

1. Introduction

1.1. Background and Previous Studies

The NASA Magnetospheric Multiscale (MMS) mission extends the investigation of magnetic reconnection in the boundary regions of the Earth's magnetosphere to the electron scale (Burch et al., 2016). In doing so, it extends the comprehensive studies of reconnection at the magnetohydrodynamic (MHD) and ion scales by previous missions to the smallest plasma scales at which the reconnection process operates. With its unprecedentedly high data rate and the smallest ever separations among four spacecraft, MMS is uniquely capable of evaluating the occurrence of various wave modes and wave-particle interactions and their importance for magnetic reconnection.

Previous observations have shown the importance of lower hybrid, Langmuir, and whistler mode waves in the vicinity of magnetopause reconnection sites (e.g., Cao et al., 2017; Fujimoto et al., 2011; Graham, Khotyaintsev, et al., 2016; Vaivads et al., 2004, 2007), and some important new insights made available by MMS have been discussed by Graham, Khotyaintsev, Norgren, et al. (2017), Graham, Khotyaintsev, Vaivads, et al. (2017), and Khotyaintsev et al. (2016). The crescent-shaped electron distributions identified by Burch et al. (2016) are shown by Graham, Khotyaintsev, Vaivads, et al. (2017) to generate upper hybrid waves in the electron diffusion region (EDR) via the beam mode. Whistler mode waves have been observed by Graham, Vaivads, et al. (2016) and Wilder et al. (2017) near the reconnection separatrix with the generation mechanism being a T_{perp}/T_{par} anisotropy although Wilder et al. showed evidence that the beam mode

Table 1
Measurements Made on Each MMS Spacecraft

	Description
FIELDS	3D electric and magnetic field measurements at $<$1 ms time resolution (DC) and waves to 6 kHz (*B*) and 100 kHz (*E*).
Fast plasma	Full sky viewing of plasma electrons and ions at 32 energies (10 eV to 30 keV): electrons in 30 ms and ions in 150 ms.
Energetic particles	Full sky viewing of ion and electron energetic particles (20–500 keV) with composition.
HPCA	Composition-resolved 3-D ion distributions (1 eV–40 keV) for H^+, He^{++}, He^+, and O^+. Full sky at 10 s.
ASPOC	Maintain S/C potential to $\leq$4 V using ion emitter.

can also produce whistler mode waves in certain parameter regimes. Lower hybrid waves have been shown to be present in the EDR because of the lower hybrid drift instability (Graham, Khotyaintsev, Norgren, et al., 2017).

1.2. Summary of Observations

The current study was motivated by the occurrence of a magnetopause crossing on 23 November 2016 with the four MMS spacecraft moving from the magnetosheath to the magnetosphere south of the X-line as indicated by the ion jets. During this event there was a unique observation of rising-tone whistler mode chorus emissions with peak frequency at the location of the transition from closed to open magnetic field lines at the electron stagnation point. As a result, the entire chorus band was located on open magnetic field lines on the magnetosphere side of the reconnection X-line. As noted by Stenberg et al. (2007), chorus waves are generally observed in closed field line regions and particularly in the equatorial dawnside magnetosphere or in magnetic minima at high latitudes (Tsurutani & Smith, 1977). As is shown in this report, MMS observed rising-tone chorus waves in a region of open field lines, as determined by the mixture of magnetosheath and magnetospheric electrons in the region of the EDR between the X-line and the electron stagnation point.

Throughout the chorus band a southward directed field-aligned beam of magnetosheath energy electrons was observed as expected for the reconnection electron jet. We show that these beams are likely the source of electron plasma oscillations that are observed at frequencies extending from above the electron cyclotron frequency (F_{ce}) to near the electron plasma frequency (F_{pe}). Also observed throughout the chorus band was a perpendicular electron temperature gradient with $T_{perp}/T_{par} \sim 1.6$, and it is this temperature gradient that is the most likely source of the whistler mode chorus waves.

On the magnetosheath side of the X-line there was another southward electron beam, which also was associated with a reconnection electron jet. These electron beams were accompanied by broadband waves that were electromagnetic at frequencies below F_{ce} and electrostatic up to 20 kHz as expected for beam-generated waves (Graham, Khotyaintsev, Vaivads, et al., 2017). The coexistence of whistler mode chorus and higher-frequency electrostatic waves in the dayside outer magnetosphere was noted by Reinleitner et al. (1983) and attributed to electron trapping and Landau acceleration of keV electrons by the whistler waves.

1.3. Analysis and Conclusions

The electron distribution function in the region where rising-band whistler mode chorus and higher-frequency electrostatic waves were observed together in the region of open field lines between the reconnection X-line and the electron stagnation region was modeled using four bi-Maxwellian distributions. A WHAMP (Waves in Homogeneous Anisotropic Multicomponent Plasma) dispersion analysis (Rönnmark, 1982) showed that the whistler mode waves were produced by the observed electron distribution, most likely from the temperature anisotropy ($Te_{perp}/Te_{par} \sim 1.6$) while the electrostatic waves resulted from a beam-plasma interaction.

Using the newly developed 7.5 ms electron moments (Rager et al., 2018), we show that the open-closed magnetic field boundary occurs just Earthward of the chorus apex in association with an electric field structure with large E_L and E_M components and $J \cdot E > 0$, indicating reconnection dissipation at the electron stagnation point.

The whistler mode result agrees with the previous work of Vaivads et al. (2007) and Stenberg et al. (2007), who observed whistlers at the high-latitude magnetopause with Cluster and associated their generation

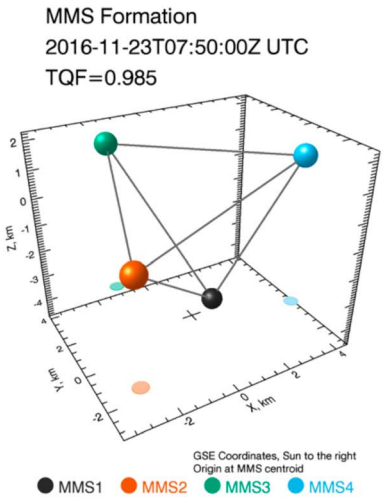

(a)

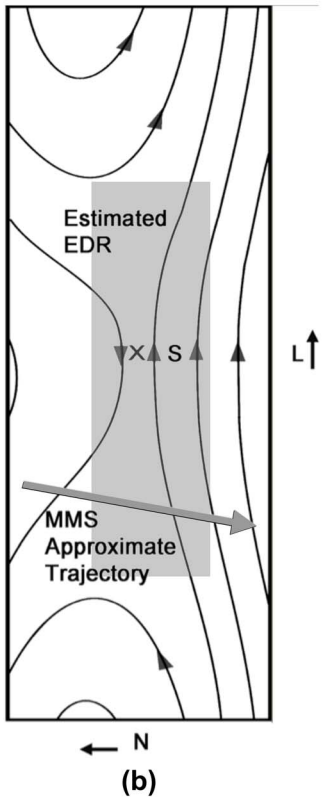

(b)

Figure 1. (a) MMS tetrahedron at 0750 UT on 23 November 2016 when spacecraft constellation was located at R = 10.27 R_E and MLT = 13.24 h. TQF is the tetrahedron quality factor with 1.0 being a regular tetrahedron. (b) Sketch of magnetic field lines for asymmetric reconnection with the magnetosheath to the left and the magnetosphere to the right. Approximate extent of the electron diffusion region is shown by the gray rectangle. Estimated trajectory of MMS through the magnetopause is shown by the gray arrow. This trajectory was caused mainly by the velocity of the magnetopause, which had an average magnitude of ~44 km/s but which oscillated in sign causing multiple magnetopause encounters. X-line and electron stagnation region are labeled by X and S, respectively. The L, M, and N components in base GSE coordinates are the following: L = [0.31690800, 0.078344800, 0.94521499], M = [0.26392251, −0.96386427, −0.0085962582], and N = [0.91691172, 0.25379226, −0.30580175].

with an electron temperature anisotropy formed by the escape of magnetospheric electrons from the first open magnetic flux tube. Graham, Vaivads, et al. (2016) drew the same conclusion for Cluster observations at the low-latitude reconnection separatrix. Thus, we can essentially confirm this explanation while also showing its correlation with the opening of magnetic field lines near the electron stagnation point where they are accompanied by higher-frequency electrostatic waves generated by reconnection electron jets.

2. Magnetospheric Multiscale Measurements

2.1. Description of MMS Measurements

The measurements made on each of the four MMS spacecraft are listed in Table 1. Especially important for reconnection is the high time resolution of the plasma measurements: 30 ms for electrons and 150 ms for ions, as compared to previous resolutions in the range of a few seconds. This improvement required the use of multiple analyzers rather than one spinning analyzer, resulting in stringent requirements on their absolute calibration and intercalibration. The unprecedented precision and accuracy of the plasma instruments allow MMS to make accurate measurements of currents and electron drift velocities in space for the first time. Another advance is the accurate measurement of three-axis electric fields with sampling frequencies up to 65,536/s. Data taken at the highest measurement resolution on MMS are referred to as burst mode data, and all instruments operate in burst mode whenever the spacecraft are beyond a geocentric distance of 9 R_E on the dayside of Earth. However, even in burst mode the 65,536/s E-field sampling frequency, which is triggered on board by signal variability, is only available about 1/3 of the time while the remainder of the burst mode data is sampled at 8,192/s. This study takes advantage of an important improvement to the plasma measurement time resolution (Rager et al., 2018), which utilizes the interleaved nature of the coverage of velocity space to yield both electron moments and distribution functions at 7.5 ms time resolution.

2.2. Overview of Observations by MMS on 23 November 2016

Analysis of three separate electron diffusion regions (EDRs) observed by MMS on 23 November 2016 has been presented by Webster et al. (2017). The subject of this report is another EDR, which was situated in time between the first and second of Webster's events. The distinguishing feature of this event is the presence of rising-tone whistler mode chorus emissions extending into the diffusion region from the magnetosphere-side separatrix.

During this event the magnetopause was moving Sunward at approximately 44 km/s, which is much faster than the spacecraft velocities of a few km/s. However, there were some oscillations in the direction of magnetopause motion resulting in the multiple encounters reported by Webster et al. (2017). Such an oscillation resulted in a dual encounter with the electron stagnation region for the time period of this study. During this time period the spacecraft were maintained in a tetrahedron configuration with an average interspacecraft separation of ~7 km as shown in

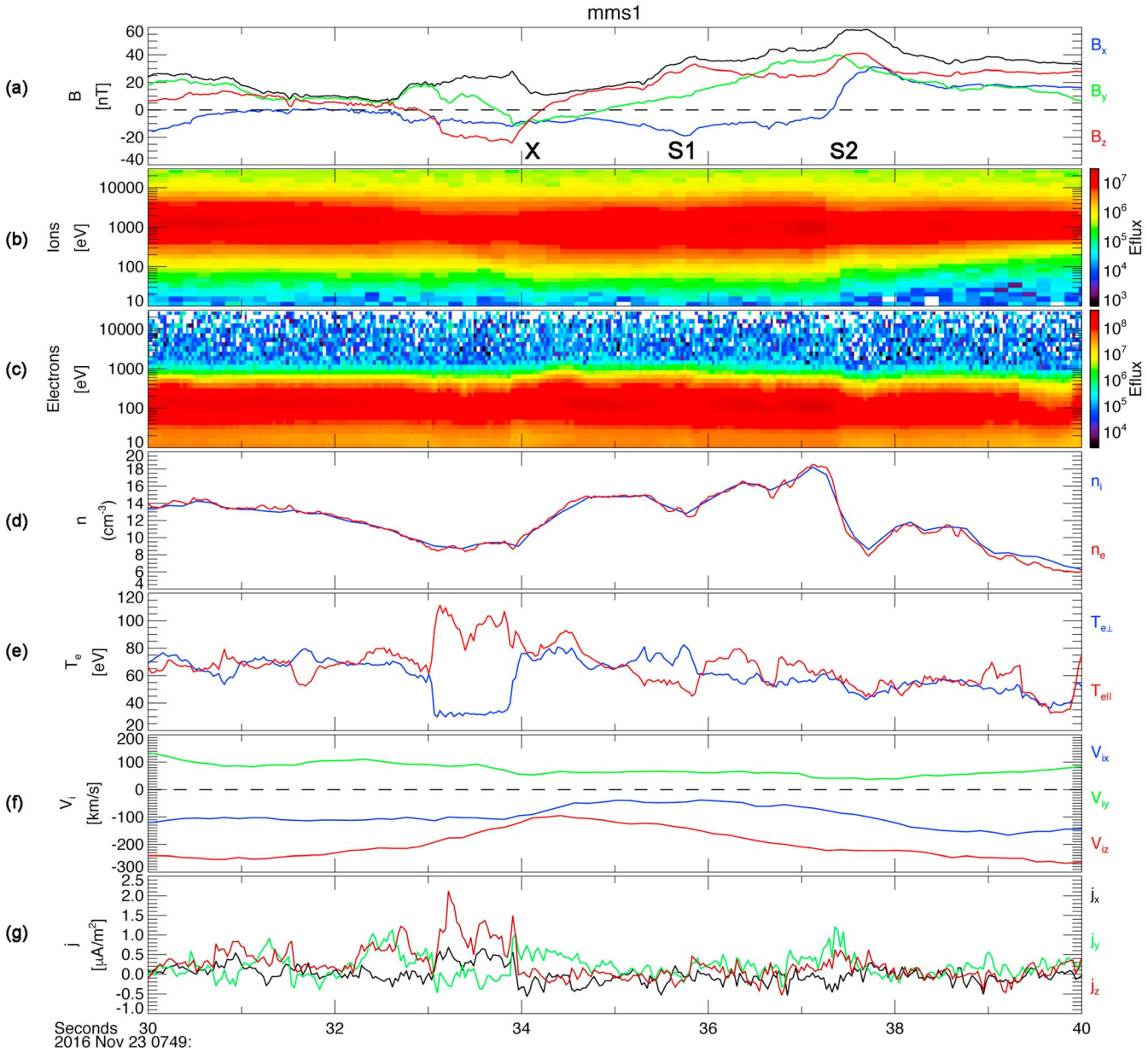

Figure 2. Overview of magnetic field and plasma data for a 10 s period on 23 November 2016. (a) Magnetic field components in GSE coordinates and total B (black trace); (b) ion energy-time spectrogram; (c) electron energy-time spectrogram; (d) ion and electron densities; (e) parallel and perpendicular electron temperatures; (f) ion velocity components; and (g) plasma current components. Nearest approaches to the X-line (based on B_Z reversal) and electron stagnation region (based on electron spectrogram) are noted in the top panel by X and S1/S2, respectively. At S1 there was a brief decrease in electron density (Figures 2c and 2d), while at S2 there was a much larger and longer-lived electron density decrease.

Figure 1, which also contains a sketch of the approximate trajectory of the MMS spacecraft through the reconnection diffusion region.

Figure 2 shows an overview of magnetic field and plasma data for a 10 s period on 23 November 2016. Noted in Figure 2a are (X) the approximate location of the closest approach to the reconnection X-line as indicated by the B_z reversal and local B minimum and (S1 and S2) the approximate locations of the electron stagnation point as indicated by the sharp reduction in energy flux in Figure 2c and the density drop in Figure 2d, which is larger and longer-lived for S2. We note in Figures 2e and 2g a very large Te_{par}/Te_{perp} and associated strong plasma currents in mostly the GSE *z* direction. Figure 2g shows another intense current in mostly the GSE *y*

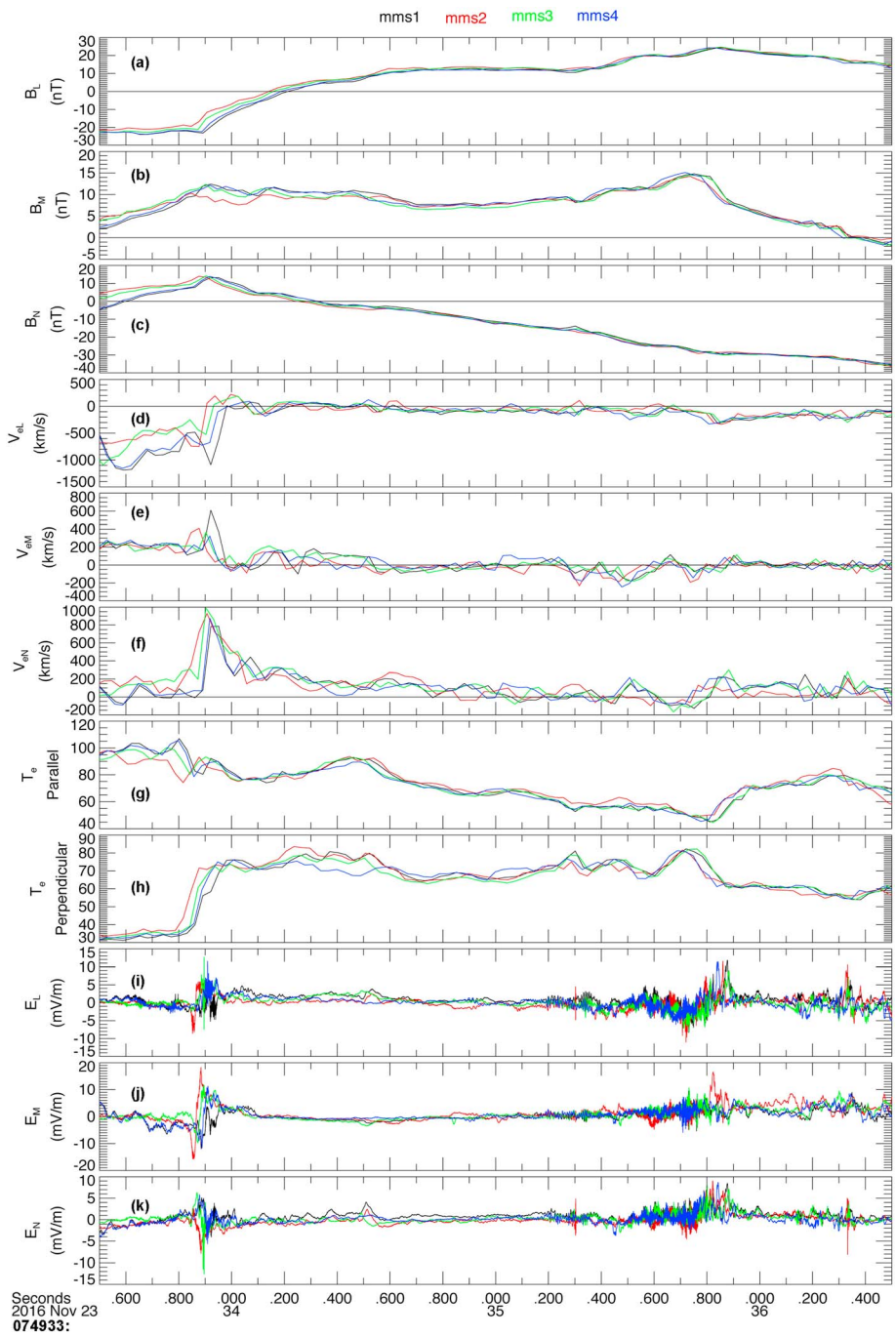

Figure 3. Multispacecraft plot of magnetic and electric fields and plasma moments on 23 November 2016 from 07:49:33.5 to 07:49:36.5 UT. Magnetic and electric field quantities are plotted in boundary-normal coordinates as defined for Figure 1. (a) B_L, (b) B_M, (c) B_N, (d) v_{eL}, (e) v_{eM}, (f) v_{eN}, (g) T_{epar}, (h) T_{eperp}, (i) E_L, (j) E_M, and (k) E_N.

direction at the second approximate electron stagnation point (S2). In this study we focus on the 3 s time period near the center of Figure 2 (between 33.5 and 36.5 s) and the region of $Te_{perp}/Te_{par} > 0$ between 35 and 36 s where rising-tone whistler mode chorus was observed.

Figure 3 shows overlayed electric and magnetic field data and plasma moments from the four MMS spacecraft for the time period from 07:49:33.5 to 07:49:36.5 UT on 23 November 2016. The electric and magnetic field data are plotted in boundary-normal coordinates as defined in the caption to Figure 1. We note the

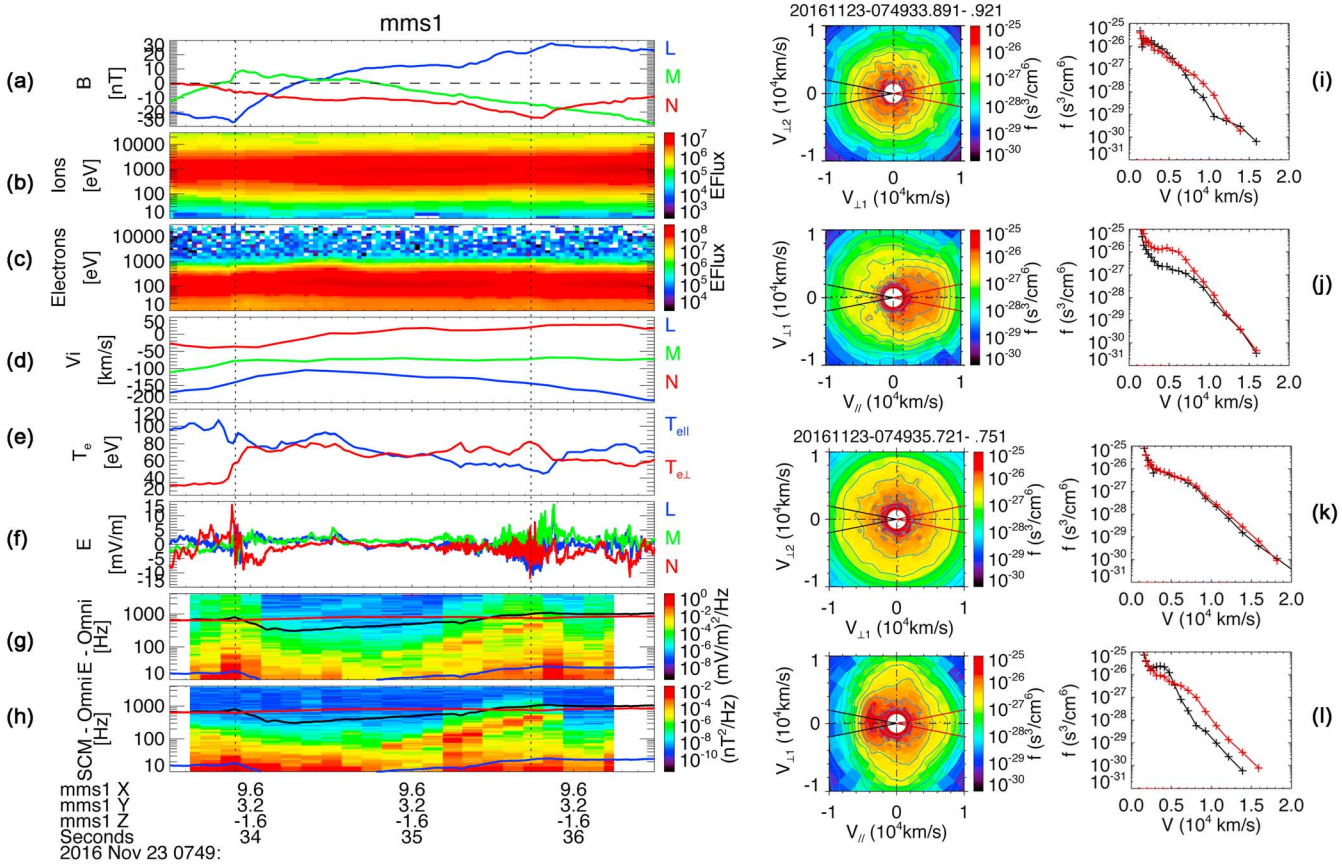

Figure 4. Overview of magnetopause crossing on 23 November 2016. (a) Magnetic field components in boundary-normal coordinates; (b) ion energy-time spectrogram; (c) electron energy-time spectrogram; (d) ion velocity; (e) electron temperature; (f) DC electric field; and (g) AC electric field frequency-time spectrogram with black, red, and blue curves denoting F_{ce}, F_{pi}, and F_{lh}; (h) AC magnetic field frequency-time spectrogram, (i) (left) polar plot centered at 07:49:33.906 UT (noted by left vertical line in left panel) of electron velocity space distribution with $v_{\perp 1}$ in the $(b \times v) \times b$ direction, which is a proxy for $E \times B$, and $v_{\perp 2}$ in the E direction. (right) Line plots in red and black showing average velocity space distributions within the red and black sectors in each polar plot. (j) Same as Figure 4i except in the plane containing the magnetic field and $v_{\perp 1}$, (k and l) same as Figures 4i and 4j except for 07:49:35.736 UT (noted by right vertical line in left panel).

close similarity of the magnetic field data from all four spacecraft, particularly in the middle part of the plot. We identify the closest approach to the reconnection X-line by the polarity reversal of B_L at approximately 07:49:34.2 UT and note the strong electric field fluctuations that occurred just upstream of this point and again near 07:49:35.8 UT, which we identify as the electron stagnation region from the rapid transition from $Te_{perp}/Te_{par} > 1$ to $Te_{perp}/Te_{par} < 1$ (Figures 2g and 2h) as well as from the electron data in Figures 2c and 2d.

Figure 4 provides an overview of the MMS1 observations from 07:49:33.5 to 07:49:36.5 UT. The left side of Figure 4, from top to bottom, shows magnetic field components, ion and electron energy-time spectrograms, ion velocity, electron temperature, electric field, electric field frequency-time spectrogram, and magnetic field frequency-time spectrogram. The *B*, *E*, and V_i plots are in boundary-normal (LMN) coordinates with transformation matrices as listed in the caption of Figure 1. MMS was initially in the magnetosheath and moved toward the magnetosphere following the B_L reversal (X-line) occurring at about 07:49:34.2 UT. Throughout the plot V_{iL} is negative, denoting locations below the reconnection midplane in the southward exhaust as sketched in Figure 1b. An electron temperature anisotropy with $Te_{perp} > Te_{par}$ is evident between 35.1 s and 35.9 s, coinciding with the rising-tone whistler mode chorus band in Figures 4g and 4h. As noted by Gary and Karimabadi (2006) such a temperature anisotropy leads to whistler mode wave growth, for example, through the whistler anistropy instability.

In Figures 4a–h two times of interest are noted by the vertical dashed lines (at 07:49:33.900 UT and 07:49:35.735 UT), and electron distribution functions (DFs) from MMS1 for these two times are shown in the right side of the figure. In Figures 4i–4l polar plots of the electron distribution functions in planes perpendicular and parallel to *B* are accompanied by line plots in two directions noted by black and red angular sectors. Each line plot is composed of the average DF within the corresponding sector. Figures 4i and 4j show that just upstream of the B_L reversal the electrons show moderate agyrotropy in the plane perpendicular to *B*, indicating the possibility of a weak crescent distribution. In the plane parallel to *B* there is an intense beam along *B*, forming a southward electron jet. Such beams are expected to produce electron plasma oscillations via a beam-plasma instability (e. g., Fuselier et al., 1985). Figure 4g shows waves at this time that are consistent with electrostatic waves extending above Fce with the electromagnetic waves at lower frequencies mainly populating the lower hybrid frequency range.

Figures 4k and 4l are taken from near the crest of the rising-tone whistler mode chorus emissions and are typical of the distribution functions throughout the chorus ramp. While the distribution perpendicular to *B* in (k) is highly gyrotropic, the v_{par}, v_{perp} plot in Figure 4l shows a reduction in T_{par} caused by the escape of magnetospheric electrons as suggested by Vaivads et al. (2007), Stenberg et al. (2007), and Graham, Vaivads, et al. (2016) and by the formation of a beam along $-v_{par}$ resulting from the incursion and subsequent field-aligned acceleration of magnetosheath electrons. We note that the line plots in Figures 4i–4l extend to 2×10^4 km/s (1,137 eV), while the polar plots only extend to 1×10^4 km/s. The black curve (at 180° average pitch angle) shows a significant decrease from the red curve (0° pitch angle) at all velocities above 0.5×10^4 km/s. This plot is very similar to Figure 4g of Graham, Vaivads, et al. (2016), which extends to higher energies. As in Graham, Vaivads, et al. (2016) we identify the higher energy particles as magnetospheric electrons, it is clear from their relatively low energies that they are most likely from the closed field line region of the low-latitude boundary layer.

While the electron temperature anisotropy ($Te_{perp}/Te_{par} > 1$) is the most likely cause of the whistler mode chorus, the low-energy beam (or electron jet) should generate electrostatic waves above F_{ce} via the electrostatic beam mode (Fuselier et al., 1985). Such waves are seen throughout the region occupied by the whistler mode chorus emissions, and these will be seen to extend to near the electron plasma frequency (F_{pe}) in a subsequent plot.

2.3. Evaluation of Ohm's Law Terms and Dissipation

The dissipative processes that occur in the reconnection diffusion region can be expressed by the electron momentum equation or generalized Ohm's law:

$$E + v \times B = \frac{m_e}{e}\frac{dv_e}{dt} - \frac{\nabla \cdot \overleftrightarrow{P_e}}{en} + \frac{J \times B}{en} + \eta J \quad (1)$$

where *E* and *B* are the vector electric and magnetic field, respectively; *J* is the vector current; v_e is the electron velocity; η is anomalous resistivity; P_e is the electron pressure tensor; m_e is electron mass; *n* is the plasma density; and *e* is the electron charge. Ideal MHD physics will occur if the right-hand side (RHS) of equation (1) is zero. If any of the terms are nonzero then MHD will be violated and reconnection might occur.

Measurements by the tetrahedron of MMS spacecraft can be used to gain insight into the sources of electric fields associated with reconnection to a greater or lesser extent depending on whether or not all four spacecraft are in the reconnection diffusion region simultaneously. The average 7 km separation among the spacecraft during the second magnetopause exploration of MMS (September 2016–March 2017) provides the best opportunity to evaluate the electric field sources. Figure 5 shows the evaluation of the terms on the right-hand side of the generalized Ohm's law and comparison with the measured electric fields for the same time period as Figure 4. Plotted in Figure 5 from top to bottom are the following: (a) vector *B* at the centroid of the four spacecraft, (b) current from curl *B*, (c) $E_{inertia} = (m_e/e)dv_e/dt$, (d) $-\mathrm{Div}\, P_e/en$, (e) $E_{Hall} = J \times B/en$, (f) the total RHS of Ohm's law, (g) $E' = E + v_e \times B$ at the centroid, (h) $J \cdot E'$ at the centroid, (i) the M component of E', and (j) the M component of the RHS of Ohm's law.

The same two vertical lines of reference as in Figure 4 are shown in Figure 5 with electron DFs at the left and right, respectively, for the two selected times. Since MMS1 DFs were plotted in Figure 4 for these same two times, DFs for only the other three spacecraft are shown in Figure 5. At the first time marker, when the

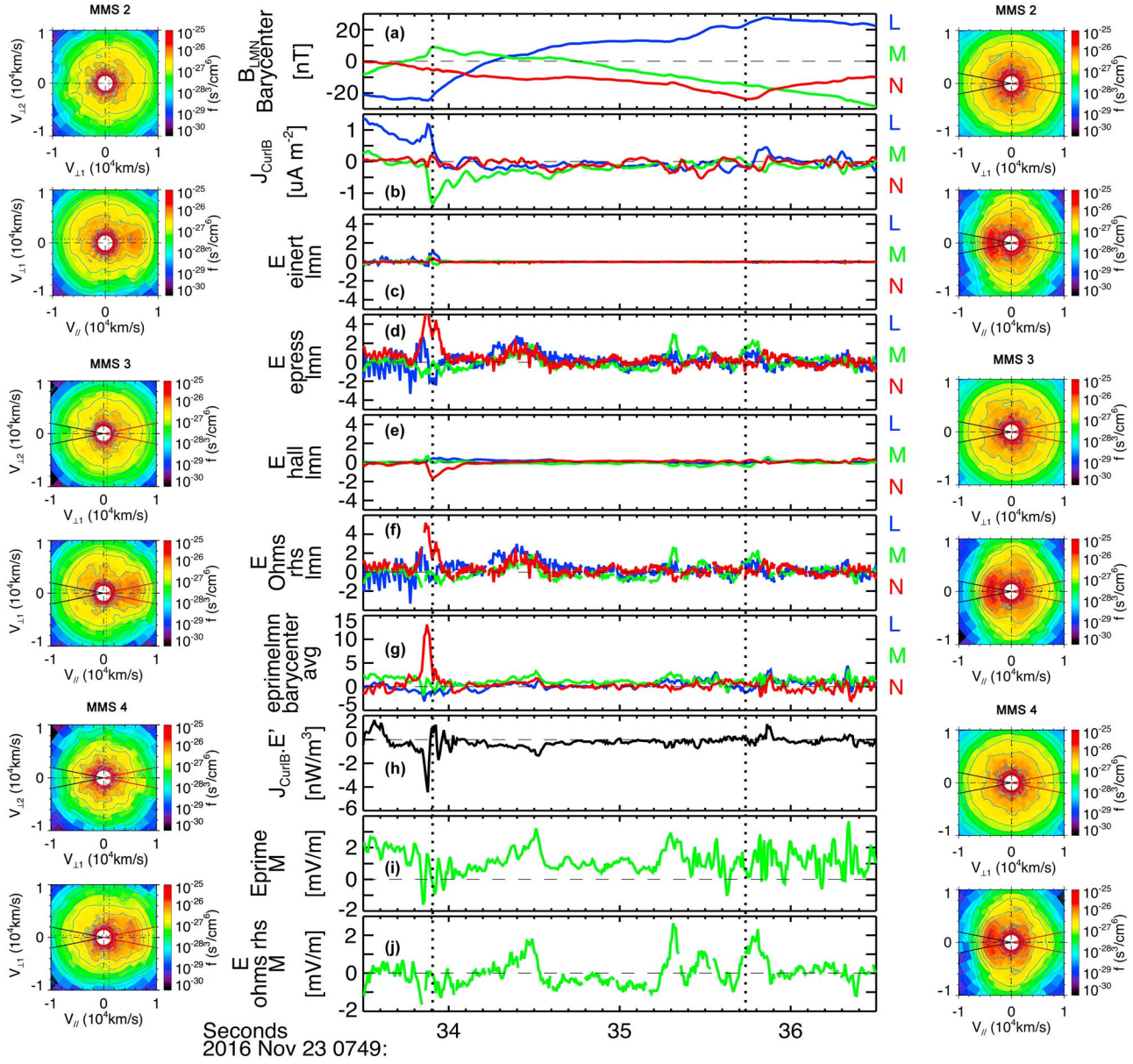

Figure 5. *Middle column*: evaluation of the terms on the right-hand side (RHS) of the generalized Ohm's law based on MMS measurements in boundary-normal coordinates. (a) Centroid magnetic field, (b) current from curl B, (c) $E_{\text{inertia}} = (m_e/e)dv_e/dt$, (d) $-\text{div}\, P_e/en$, (e) $E_{\text{Hall}} = J \times B/en$, (f) RHS of Ohm's law, (g) E' ($E + v_e \times B$) at barycenter, (h) $J \cdot E'$, (i) E_M, and (j) M component of RHS of Ohm's law. *Left column*: DF polar plots from MMS2, MMS3, and MMS4 at time of left vertical line with format the same as for Figures 3i and 3j). *Right column*: Same as left panel except for the time at the right vertical line.

spacecraft were located just upstream of the B_L reversal (closest to the X-line), the DFs in the perpendicular plane for MMS2 and MMS3 show agyrotropic distributions resembling the crescent-shaped distributions described by Burch et al. (2016). The perpendicular-plane DF for MMS4 shows a generally gyrotropic distribution as was the case for MMS1 (in Figure 4), while in the plane containing B all four spacecraft detected intense electron beams along $+v_{\text{par}}$, which is indicative of a southward reconnection jet with a source in the X-line region. As indicated by the DFs from two of the spacecraft (MMS2 and MMS3), they were near or within the upstream edge of the EDR, and this conclusion is supported by the line plots in Figure 5 (middle column). At the first vertical time marker Figure 5g shows the strongest E' component being E_N while the strongest currents (Figure 5b) are directed along $-$M and +L. Comparison of Figures 5i and j shows that E_N is generally well predicted by the RHS of Ohm's law with the strongest contribution being from the pressure tensor divergence (Figure 5d) with a significant Hall-field

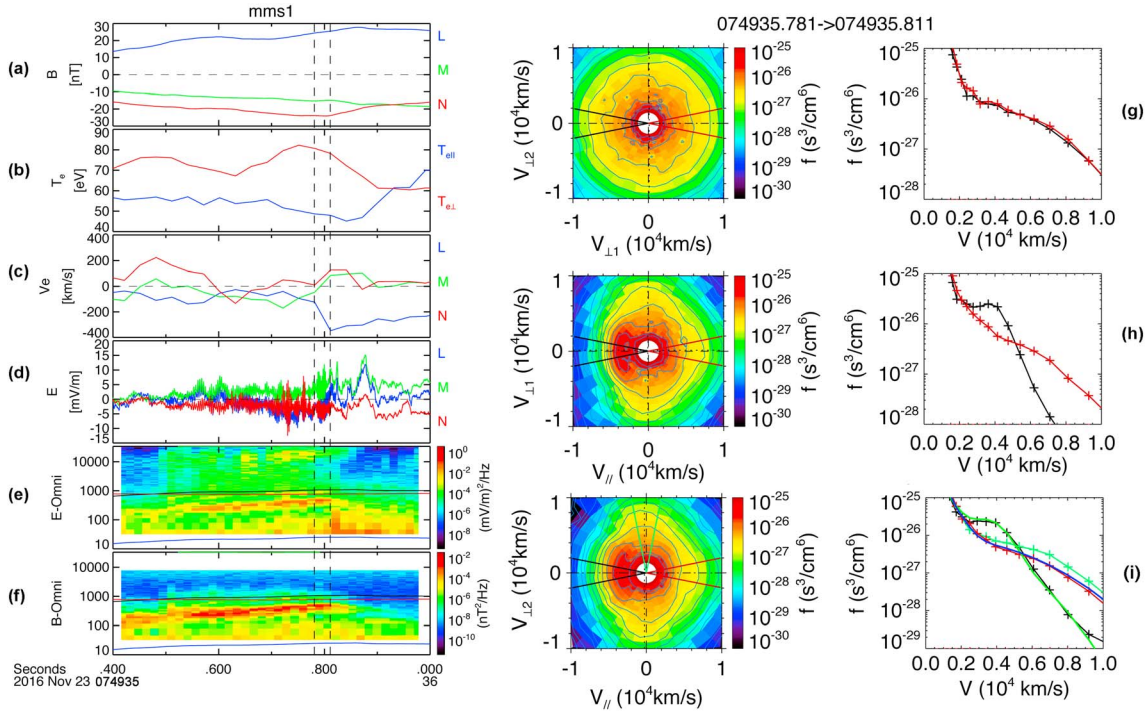

Figure 6. High-rate data from MMS1 on 23 November 2016 in boundary-normal coordinates: (a) vector magnetic field; (b) electron temperature, T_{par} in blue and T_{perp} in red; (c) electron velocity; (d) DC electric field at 8,192/s; (e) frequency-time spectrogram of AC electric field data; (f) frequency-time spectrogram of AC magnetic field data; (g) same as Figure 3(i) except for 07:49:35.796 UT; (h) same as Figure 3 (j) except for 07:49:35.796 UT; (i) polar plot of electron velocity space distribution with the horizontal axis along *B* and the vertical axis ($v_{\perp 2}$) with cuts through the distributions shown for the field-aligned sectors shown in black and red on the polar plots and for Figure 6i an additional cut along $v_{\perp 2}$. Correction for the spacecraft potential of 4.4 V and a four bi-Maxwellian fit to the field-aligned distributions is added to Figure 6i with (1) a stationary background population with $T = 6$ eV, $n = 3$ cm^{-3}, and $T_{perp}/T_{par} = 1$, (2) a drifting Maxwellian with $T = 4$ eV, $n = 1.0$ cm^{-3}, $T_{perp}/T_{par} = 4.0$, and $V_{drift}/V_{th} = -2.95$ (flow along $-B$), (3) a drifting Maxwellian with $T = 60$ eV, $n = 5$ cm^{-3}, $T_{perp}/T_{par} = 2.2$, and $V_{drift}/V_{th} = 0.28$, and (4) a stationary population with $T = 45$ eV, $n = 1$ cm^{-3}, and $T_{perp}/T_{par} = 1$. The green curve fit in Figure 6i is the sum of (1), (2), and (4), while the blue curve is the sum of (1), (3), and (4). The purpose of showing the 90° distribution (the green data, which are not included in the field-aligned fits) is to illustrate the source of the T_{perp}/T_{par} anisotropy shown in the line plot in Figure 6b.

contribution with the opposite polarity (Figure 5e). Between the two vertical lines E_M is also well predicted as shown with an expanded vertical scale in Figures 5i and 5j.

Referring to the second time marker in Figure 5, which is in the region of electron stagnation on the magnetosphere side of the X-line and also near the apex of the rising-tone whistler mode chorus emissions, we see that electron DFs from all four spacecraft are similar and as described for Figure 4 with a beam (southward electron jet) along $-v_{par}$ and magnetospheric electrons flowing along $+v_{par}$. As noted in the discussion of Figure 4l, the perpendicular temperature gradient appears to be supported by escape of magnetospheric electrons along a recently opened magnetic field line. Although only weak electric fields and dissipation are observed at the time marker, there is a significant dissipation peak at about 0.1 s later, and this peak will be shown to have existed at all four spacecraft in the next two figures.

3. Wave Generation Mechanisms

3.1. Wave Data Description

Figure 6 shows a detailed view of magnetic and electric fields, high-rate electric and magnetic wave data, and electron distribution functions for a 0.6 s time period beginning at 07:49:35.4 on 23 November 2016. Plotted in Figures 6a–6f are *B*, T_e, v_e, *E*, and E and B frequency-time spectrograms using sample rates of 65,536/s and 16,384/s, respectively. F_{ce}, F_{pi}, and F_{lh} are plotted in black, red, and blue, respectively. F_{uh} (upper hybrid frequency) is located just off the top of the plots at about 28 kHz. The two dashed vertical lines at 074935.781 and 074935.811 UT note the time range of the DF plots in the right side of Figure 6, which have the same format as used in Figure 4. As in Figure 4, the DF in the perpendicular plane (Figure 4g) is gyrotropic while

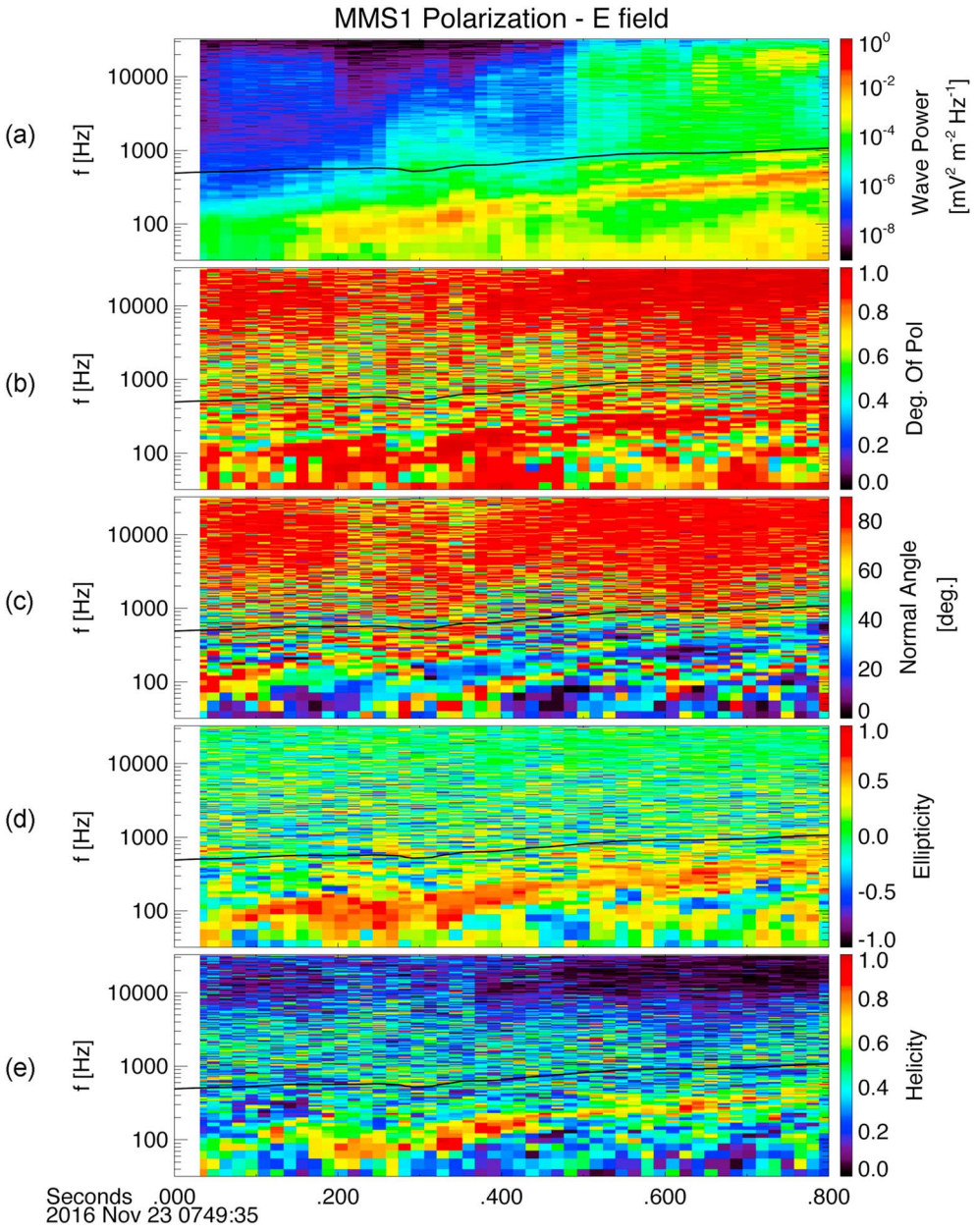

Figure 7. Results of electric field polarization analysis: (a) electric power spectral density (PSD) versus frequency, (b) degree of polarization, (c) wave normal angle, (d) wave ellipticity, and (e) wave helicity.

in both parallel cuts shown in (Figures 4h and 4i) the same loss of high-energy electrons is noted, which causes $Te_{perp}/Te_{par} > 0$ as seen clearly in Figure 4b.

3.2. Polarization Analysis

As noted by Gary and Karimabadi (2006) an electron temperature anisotropy is a likely cause of whistler mode emissions, including the chorus-type emission shown in Figure 6, which coincides with the significant temperature anisotropy shown in Figure 6b. Based on the previous results of Fuselier et al. (1985) and Graham, Khotyaintsev, Vaivads, et al. (2017), we expect the high-frequency electrostatic waves to be associated with beam-plasma instabilities. Thus, we performed a polarization analysis and a dispersion analysis in order to determine the characteristics and generation mechanisms for the whistler mode waves and higher-frequency electrostatic waves. Figure 7 shows the E-field polarization analysis for the 0.8 s time period starting at 074935 UT. Figure 7a repeats the electric field wave power spectrogram showing the upper and lower

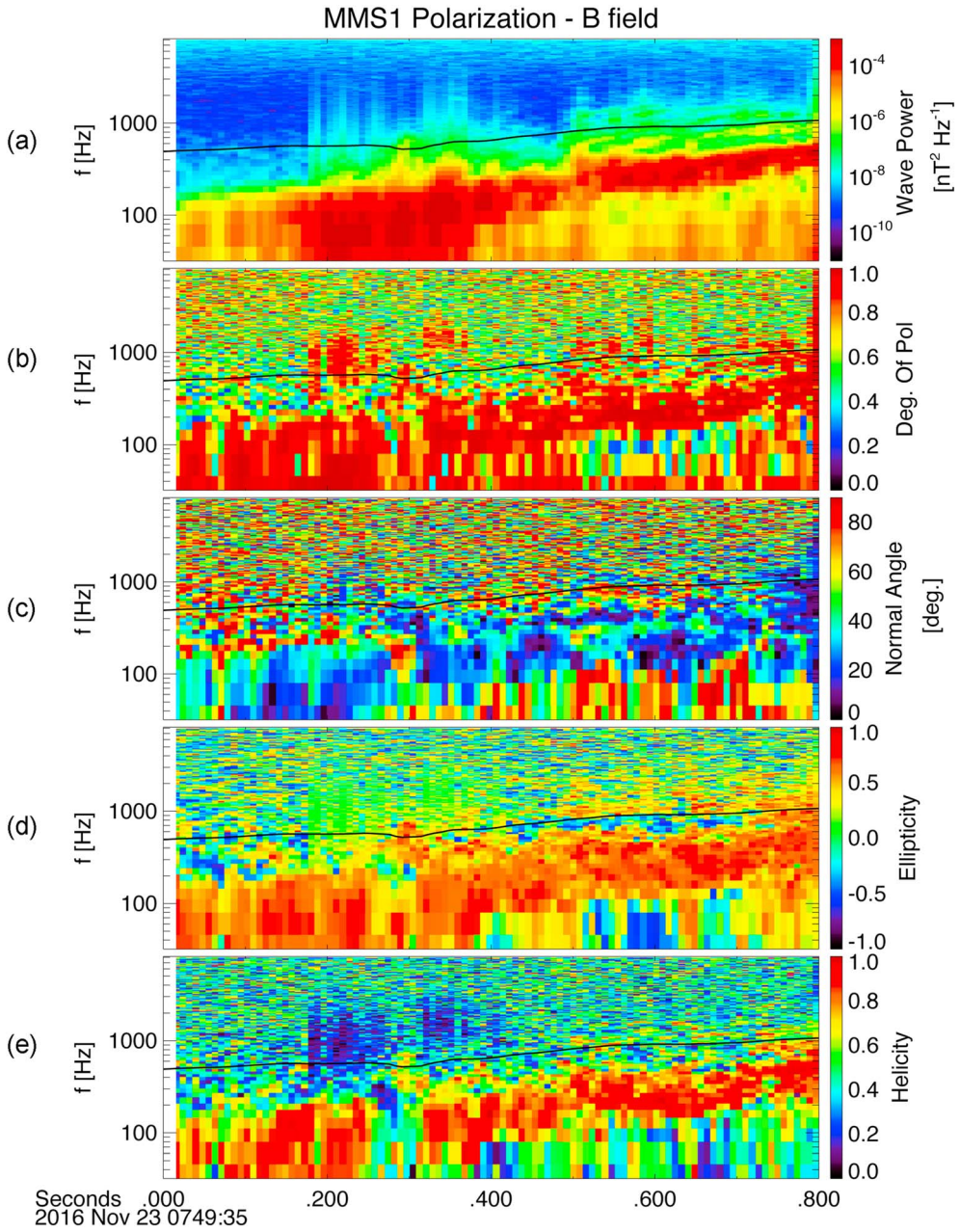

Figure 8. Same as for Figure 6 except for magnetic field.

bands of whistler mode chorus and the electrostatic waves near and above 10 kHz, with these features appearing more clearly in the second half of the plot. Figure 7b shows the degree of polarization to be near 1.0 for the electrostatic waves and lower band chorus and also for the upper band chorus where it is most intense. The wave-normal angle in Figure 7c shows values near 0° (field aligned) for the lower band chorus but becoming more oblique for the upper band. Both the ellipticity and the helicity show fairly high positive values for the lower band chorus (right handed and nearly circular), while the results are less clear for the upper band. Such differences between the lower and upper chorus bands are well known and have recently been analyzed by Li et al. (2013).

Similar results for the B field are shown in Figure 8. An interesting feature in Figure 8a is the connection (or bridge) between the upper and lower chorus bands that occurs at three different times between 0.5 s and

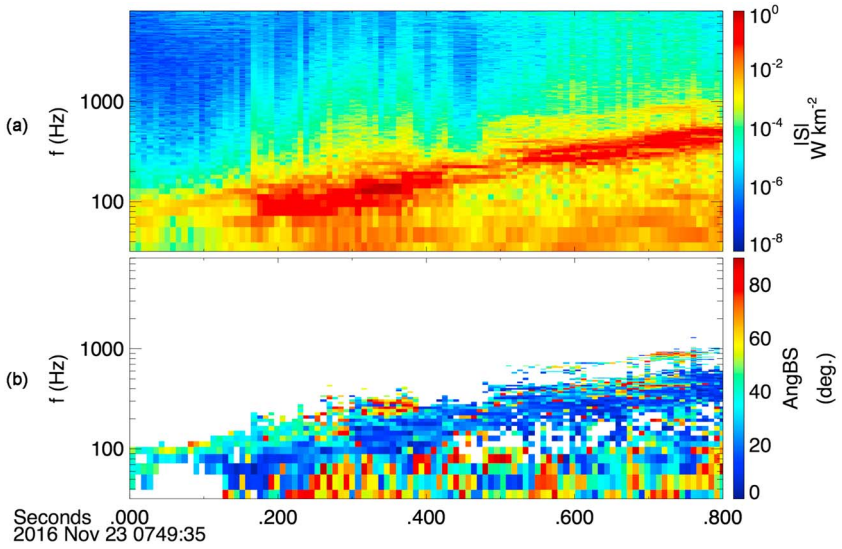

Figure 9. (a) Poynting flux magnitude versus frequency for MMS1 at same time period as for Figures 6 and 7. (b) Angle between *B* and *S* (the Poynting vector) showing that the lower band chorus waves are parallel propagating (<20°), while the upper band waves tend to be more oblique (>60°).

0.7 s, which show the upper part of the lower band rising in frequency to form the upper band. We note that Kurita et al. (2012) have reported instances from THEMIS (Time History of Events and Macroscale Interactions during Substorms) of chorus without a 0.5 F_{ce} gap. In addition, the magnetic ellipticity and helicity are shown in Figures 8d and 8e to have values close to 1.0 indicating circular polarization for the lower chorus band but changing to zero helicity and negative ellipticity near F_{ce} indicating left-hand polarization, which may be a reflection or cutoff effect needing further investigation.

The results of a Poynting flux analysis of the whistler mode chorus waves are shown in Figure 9 where Figure 9a shows the magnitude of the Poynting flux while Figure 9b shows the angle between *B* and the Poynting vector. We conclude from Figure 9 that while the lower band chorus waves are propagating primarily parallel to *B* (AngBS $<$ 20°) the upper band waves tend to be more oblique with AngBS $>$ 60° for some intervals.

3.3. Dispersion Analysis

In order to investigate the causes of the observed whistler mode and electrostatic waves we used the program WHAMP (Rönnmark, 1982), which performs a linear dispersion analysis for multiple drifting bi-Maxwellian plasmas. Plotted in Figure 6i is a green curve and a blue curve that were derived from a fit to the parallel component of four bi-Maxwellian distributions: (1) a stationary background population with T = 6 eV, n = 3 cm^{-3} and T_{perp}/T_{par} = 1, (2) a drifting Maxwellian with T = 4 eV, n = 1.0 cm^{-3} T_{perp}/T_{par} = 4.0 and V_{drift}/V_{th} = −2.95 (flow along −*B*), (3) a drifting Maxwellian with T = 60 eV, n = 5 cm^{-3}, T_{perp}/T_{par} = 2.2 and V_{drift}/V_{th} = 0.28, and (4) a stationary population with T = 45 eV, n = 1 cm^{-3}, and T_{perp}/T_{par} = 1. The green curve (antiparallel to B) in Figure 6i is the sum of (1), (2), and (4), while the blue curve (parallel distribution) is the sum of (1), (3), and (4). The purpose of showing the 90° distribution (the green curve, which as expected is not reproduced by the parallel fit) is to illustrate the source of the T_{perp}/T_{par} anisotropy shown in the line plot in Figure 6b. The features in Figures 6g–6i persisted throughout the time period containing the whistler mode chorus emissions (07:49:35.40–07:49:35.84 UT), and the four-Maxwellian fit is valid throughout that region.

Figure 10 shows the dispersion relation and normalized growth rate versus wave number and frequency for the four-Maxwellian model. Figures 10a and 10c show the dispersion relation (blue curve) and normalized growth rates (red curves) for whistler mode waves. The characteristic growth-rate peak near 0.5 F_{ce} is clearly seen in Figure 10c as is the sharp drop at higher frequencies.

Results for the higher-frequency electrostatic waves are shown in Figures 10b and 10d. Positive wave growth (imaginary frequency component greater than 0) is shown for $k_\perp = 0$ (parallel propagation) over a range of $k_\parallel$

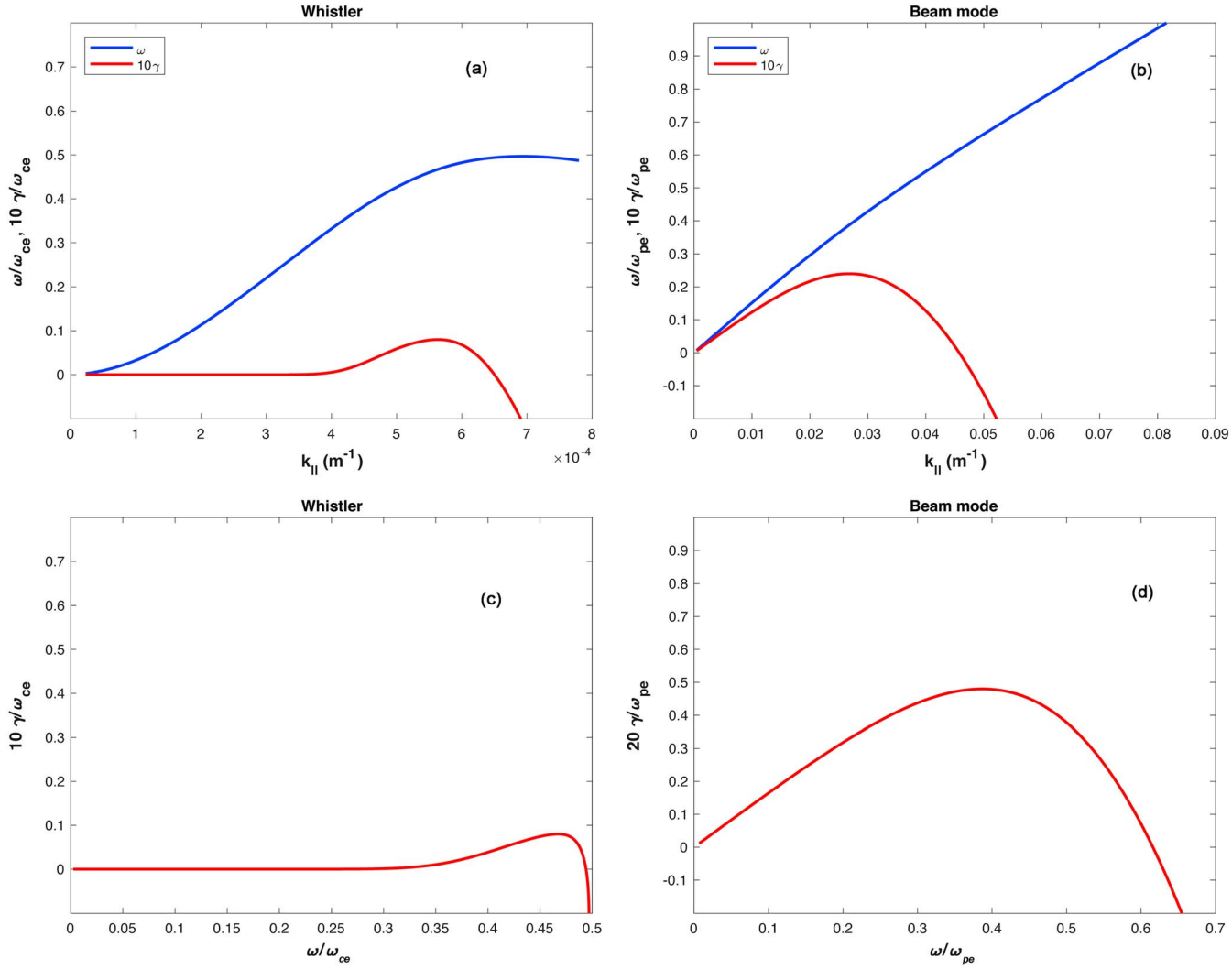

Figure 10. Results of a dispersion analysis for the electron distribution shown in Figure 6i. Four bi-Maxwellian distributions, as described in the text and the caption of Figure 6, were used as input to a WHAMP analysis (Rönnmark, 1982). (a and c) Results for the whistler mode. (b and d) Beam mode results for electrostatic waves. Results are for parallel propagation ($k_\perp = 0$) with the dispersion relations shown by the blue curves and the normalized growth rates by the red curves.

values from 0 to ~0.05 m^{-1}, while for larger values strong damping is observed. The dispersion relation in Figure 10b has the characteristic shape of waves generated by the unstable beam mode (Dum, 1989). Finally, Figure 10d plots the wave growth versus frequency with a broad peak centered at ~0.4 F_{pe}.

A plot of electric power spectral density for the time of the distribution functions shown in Figure 6 appears in Figure 11. Noted in Figure 12 are the plasma frequency (F_{pe}) and the frequency of peak wave growth from Figure 10. The peak signal is also shown by the yellow pixels in the electric field wave spectrogram in Figure 6a. The electric and magnetic field wave spectrograms in Figure 6 show clearly the lower band and upper band of the whistler mode chorus emissions along with the well-known gap near 0.5 F_{ce} (e.g., Kurita et al., 2012). The fact that there is no wave growth shown in Figure 10 near F_{ce} while a peak power spectral density at frequencies just below F_{ce} is shown in Figure 11 supports the idea that a different wave generation process may be responsible for the upper band (Li et al., 2013). We note the similarity of Figure 11 to Figure 3 of Reinleitner et al. (1983) who attributed the coexistence of chorus waves and higher-frequency electrostatic waves in the dayside outer magnetosphere to the trapping of electrons within the whistler waves and their acceleration into beams by Landau resonance.

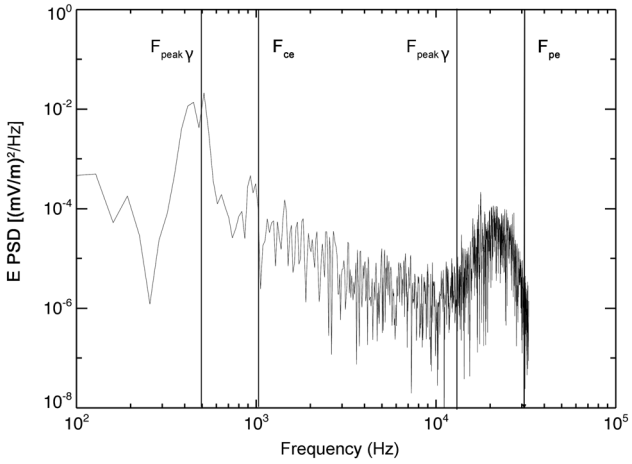

Figure 11. Electric field power spectral density measured by MMS1 for the 30 ms time period beginning at 07:49:35.77 on 23 November 2016. The frequency at peak growth from the dispersion analysis and the electron plasma frequency are noted by the vertical lines. Note the lower chorus band near 500 Hz and the upper chorus band between 900 and 1,000 Hz.

4. Dissipation at the Electron Stagnation Point

4.1. Highest Resolution MMS Data

Beginning just after the crest of the chorus event, the character of the *E* signal in Figure 6d changed to an intense positive pulse of mostly E_L and E_M reaching up to 15 mV. This pulse resulted in significant dissipation as measured by $J \cdot E'$ as shown in Figure 12, which is a zoom-in to an 0.08 s interval of Figure 6 when MMS1 had moved Earthward of the whistler mode chorus and electrostatic wave emissions. Figure 12a plots the electric field in boundary-normal coordinates at the burst mode rate of 8,192/s, while Figure 12b shows the LMN components of the current measured by FPI at the enhanced rate of 7.5 ms for electrons and 37.5 ms for ions (Rager et al., 2018). The data points are plotted every 7.5 ms with the ion portion of the current interpolated to the faster electron sample rate. Figure 12c shows a peak of dissipation measured by $J \cdot (E + v_e \times B)$, which uses the current measured by the electron and ion distributions and *E* averaged over the 7.5 ms electron (and current) time resolution. The peak dissipation shown in Figure 12c is consistent with that shown in Figure 5h for the barycenter $E + v_e \times B$ and J_{CurlB} derived for all four spacecraft.

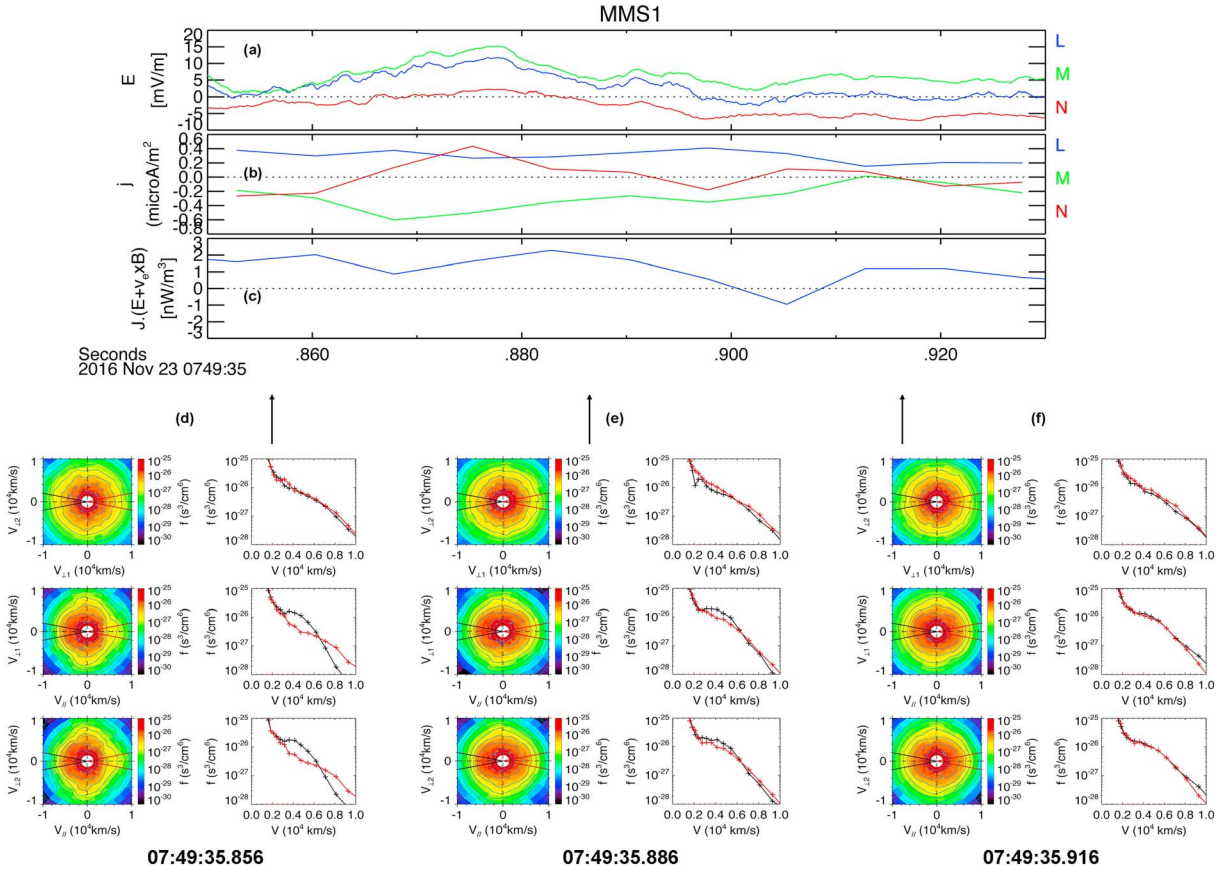

Figure 12. (a) DC electric field at 8192/s in boundary-normal coordinates, (b) current from electron and ion measurements at 7.5 ms resolution in boundary-normal coordinates with ion currents (37.5 ms resolution) interpolated to match electron time resolution, (c) dissipation measured by $J \cdot (E + v_e \times B)$ at 7.5 ms resolution with average *E*. (d–f) electron velocity space distribution function in field-aligned coordinates in (top) the plane normal to *B* with $v_{\perp 1}$ in the $(b \times v) \times b$ direction, which is a proxy for $E \times B$ and, and $v_{\perp 2}$ in the *E* direction, with red and black lines showing sectors where distribution function cuts are made, (middle) the plane containing *B* and $v_{\perp 1}$, (bottom) the plane containing *B* and $v_{\perp 2}$.

4.2. Opening of Magnetic Field Lines

Referring to the sequence of three electron DF plots shown in Figures 12d–12f, we note that (1) the electron jet beam along $-v_{\|}$ becomes weaker while the higher energy electron fluxes along $-v_{\|}$ become stronger until by Figure 12f the fluxes are essentially equal along both field-aligned directions indicating closed field lines. We conclude that the field lines opened up via reconnection at a time near the center of Figure 12 when the dissipation was highest.

While a crescent-shaped distribution (Burch et al., 2016) was observed in the DF plane perpendicular to *B* (particularly with MMS2 and MMS3) in the region just upstream of the X-line (Figure 5), no such crescents were observed in the electron stagnation region shown in Figure 12. This absence of crescent distributions could have resulted from the strong positive E_L and J_L and to a lesser extent the positive E_N and J_N as shown in Figures 12a and 12b.

We note that electron crescent distributions were observed by MMS2 and MMS3 just upstream of the X-line (Figure 5). As shown in Figure 5g, there was a strong E_N component at the time of the crescent observation. As noted by Burch et al. (2016), acceleration of magnetosheath electrons across a plasma boundary (in that case the electron stagnation point) is an important mechanism for accelerating electrons into crescent distributions. The observation of crescents on the magnetosheath side of the X-line in a region of strong E_N suggests that the same mechanism can occur at different types of boundaries such as reconnection separatrices.

5. Summary and Conclusions

5.1. Summary of Observations

On 23 November 2016 MMS made multiple magnetopause crossings between 07:49 and 07:51 UT. Three of these crossings have been analyzed by Webster et al. (2017). The current study addresses a fourth crossing that occurred between 07:49:33.5 and 07:49:36.5 UT with a focus on reconnection dissipation near the X-line and near the electron stagnation point, which bracket the electron diffusion region, and on wave phenomena and beam-plasma interactions that occurred between these two locations. During this event the four MMS spacecraft were maintained in a tetrahedron formation with the closest average separation (7 km) that was implemented during Phase 1 (dayside magnetopause) of the mission. Within the region between the X-line and the electron stagnation point the magnetic field data from the four spacecraft remained nearly identical, which was ideal for the generalized Ohm's law analysis that was performed using plasma moments and electric and magnetic field data. As shown in Figure 5f, for this event there were unusually strong E_M and E_N components extending Earthward of the peak positive E_L component (near the electron stagnation region). Two regions of interest were identified: one near 07:49:33.9 UT, just Sunward of the X-line, as defined by the sign reversal of B_L, and the other near 07:49:35.8 near the electron stagnation point as indicated by a sharp increase in Te_{perp} and decrease in Te_{par}.

5.2. Ohm's Law Analysis

Near the X-line the strongest electric field signal and the best correlation with Ohm's law terms (Figure 5) was found for E_N, which was primarily caused by the divergence of the electron pressure tensor. Similarly, in the space between the two regions of interest there was very good correlation between the measured E_M and that derived from divergence of the electron pressure tensor. Calculation of $J \cdot (E + v_e \times B)$ using data from all four spacecraft at their barycenter indicated reconnection dissipation at each region of interest with the out-of-plane current as shown in Figure 5b at the first region being associated with crescent-shaped distributions primarily at MMS2 and MMS3. The dissipation at the second region was associated primarily with magnetic field-aligned currents and electric fields (Figure 12).

5.3. Wave Analysis

Most of the space between the two regions of interest was filled with significant wave activity including (1) electromagnetic lower hybrid waves, (2) rising-tone whistler mode chorus, and (3) broadband electrostatic waves extending from F_{ce} to near F_{pe}. This space was also characterized by field-aligned electron beams, which we identify as electron jets moving southward from the X-line and by electron anisotropy with typical $Te_{perp}/Te_{par} \sim 1.6$. We showed via WHAMP dispersion analysis that the whistler mode chorus waves result from the electron temperature anisotropy, and the electron plasma oscillations resulted from a beam-

plasma instability driven by the electron jets coupled with the counterstreaming beams of magnetospheric electrons. By inspection of the electron distribution functions we confirmed a previous result from Cluster (Graham, Vaivads, et al., 2016; Stenberg et al., 2007; Vaivads et al., 2007) that the electron temperature anisotropy responsible for the whistler waves is caused by the escape of magnetospheric electrons into the magnetosheath.

5.4. Determination of Field Line Opening

Finally, we demonstrated by measurement of $J \cdot (E + v_e \times B)$ and by the observation of a mixture of magnetosheath and magnetosheric electrons within a flux tube that the onset of both the whistler waves and the whistler mode chorus waves on the Earthward side of the electron diffusion region is coincident with the opening of magnetic field lines via reconnection.

Acknowledgments
This work was supported by NASA contract NNG04EB99C at SwRI. Helpful discussions with Love Alm and Douglas Menietti are gratefully acknowledged. The entire MMS data set is available online at https://lasp.colorado.edu/mms/sdc/public/links/. Fully calibrated data are placed online at this site within 30 days of their transmission to the MMS Science Operations Center. The data are archived in the NASA Common Data Format (CDF) and so can be plotted using a number of different data display software packages that can use CDF files. A very comprehensive system called the Space Physics Environment Data Analysis System (SPEDAS) is available by downloading http://themis.ssl.berkeley.edu/socware/bleeding_edge/ and selecting spdsw_latest.zip. Training sessions on the use of SPEDAS are held on a regular basis at space physics-related scientific meetings. All of the data plots in this paper were generated with SPEDAS software applied to the publicly available MMS database, so they can readily be duplicated.

References

Burch, J. L., Torbert, R. B., Phan, T. D., Chen, L. J., Moore, T. E., Ergun, R. E., … Chandler, M. (2016). Electron-scale measurements of magnetic reconnection in space. *Science*, *352*(6290), aaf2939. https://doi.org/10.1126/science.aaf2939

Cao, D., Fu, H. S., Cao, J. B., Wang, T. Y., Graham, D. B., Chen, Z. Z., … Burch, J. L. (2017). MMS observations of whistler waves in electron diffusion region. *Geophysical Research Letters*, *44*, 3954–3962. https://doi.org/10.1002/2017GL072703

Dum, C. T. (1989). Transition in the dispersive properties of beam-plasma and two-stream instabilities. *Journal of Geophysical Research*, *94*, 2429–2442. https://doi.org/10.1029/JA094iA03p02429

Fujimoto, M., Shinohara, I., & Kojima, H. (2011). Reconnection and waves: A review with a perspective. *Space Science Reviews*, *160*(1-4), 123–143. https://doi.org/10.1007/s11214-011-9807-7

Fuselier, S. A., Gurnett, D. A., & Fitzenreiter, R. J. (1985). The downshift of electron plasma oscillations in the electron foreshock region. *Journal of Geophysical Research*, *90*, 3935–3946. https://doi.org/10.1029/JA090iA05p03935

Gary, S. P., & Karimabadi, H. (2006). Linear theory of electron temperature anisotropy instabilities: Whistler, mirror, and weibel. *Journal of Geophysical Research*, *111*, A11224. https://doi.org/10.1029/2006JA011764

Graham, D. B., Khotyaintsev, Y. V., Norgren, C., Vaivads, A., André, M., Lindqvist, P. A., … Burch, J. L. (2016). Electron currents and heating in the ion diffusion region of asymmetric reconnection. *Geophysical Research Letters*, *43*, 4691–4700. https://doi.org/10.1002/2016GL068613

Graham, D. B., Khotyaintsev, Y. V., Norgren, C., Vaivads, A., André, M., Toledo-Redondo, S., … Burch, J. L. (2017). Lower hybrid waves in the ion diffusion and magnetospheric inflow regions. *Journal of Geophysical Research: Space Physics*, *122*, 517–533. https://doi.org/10.1002/2016JA023572

Graham, D. B., Khotyaintsev, Y. V., Vaivads, A., Norgren, C., André, M., Webster, J. M., … Russell, C. T. (2017). Instability of agyrotropic electron beams near the electron diffusion region. *Physical Review Letters*, *119*(2), 025101. https://doi.org/10.1103/PhysRevLett.119.025101

Graham, D. B., Vaivads, A., Khotyaintsev, Y. V., & André, M. (2016). Whistler emission in the separatrix regions of asymmetric magnetic reconnection. *Journal of Geophysical Research: Space Physics*, *121*, 1934–1954. https://doi.org/10.1002/2015JA021239

Khotyaintsev, Y. V., Graham, D. B., Norgren, C., Eriksson, E., Li, W., Johlander, A., … Burch, J. L. (2016). Electron jet of asymmetric reconnection. *Geophysical Research Letters*, *43*, 5571–5580. https://doi.org/10.1002/2016GL069064

Kurita, S., Katoh, Y., Omura, Y., Angelopoulos, V., Cully, C. M., le Contel, O., & Misawa, H. (2012). THEMIS observation of chorus elements without a gap at half the gyrofrequency. *Journal of Geophysical Research*, *117*, A11223. https://doi.org/10.1029/2012JA018076

Li, W., Bortnik, J., Thorne, R. M., Cully, C. M., Chen, L., Angelopoulos, V., … LeContel, O. (2013). Characteristics of the Poynting flux and wave normal vectors of whistler-mode waves observed on THEMIS. *Journal of Geophysical Research: Space Physics*, *118*, 1461–1471. https://doi.org/10.1002/jgra.50176

Rager, A. C., Dorelli, J. C., Gershman, D. J., Uritsky, V., Avanov, L. A., & Torbert, R. B. (2018). Electron crescent distributions as a manifestation of diamagnetic drift in an electron scale current sheet: Magnetospheric multiscale observations using new 7.5 ms fast plasma investigation moments. *Geophysical Research Letters*, *45*. https://doi.org/ 10.1002/2017GL076260

Reinleitner, L. A., Gurnett, D. A., & Eastman, T. E. (1983). Electrostatic bursts generated by electrons in landau resonance with whistler mode chorus. *Journal of Geophysical Research*, *88*, 3079–3093. https://doi.org/10.1029/JA088iA04p03079

Rönnmark, K. (1982). WHAMP: Waves in homogeneous, anisotropic, multicomponent plasmas, Tech. Rep., pp. 1–55, Kiruna Geophys. Inst., Kiruna, Sweden.

Stenberg, G., Oscarsson, T., André, M., Vaivads, A., Backrud-Ivgren, M., Khotyaintsev, Y., … Décréau, P. M. E. (2007). Internal structure and spatial dimensions of whistler wave regions in the magnetopause boundary layer. *Annales Geophysicae*, *25*(11), 2439–2451. https://doi.org/10.5194/angeo-25-2439-2007

Tsurutani, B. T., & Smith, E. J. (1977). Two types of magnetospheric ELF chorus and their substorm dependences. *Journal of Geophysical Research*, *82*, 5112–5128. https://doi.org/10.1029/JA082i032p05112

Vaivads, A., André, M., Buchert, S. C., Wahlund, J.-E., Fazakerley, A. N., & Cornilleau-Wehrlin, N. (2004). Cluster observations of lower hybrid turbulence within thin layers at the magnetopause. *Geophysical Research Letters*, *31*, L03804. https://doi.org/10.1029/2003GL018142

Vaivads, A., Santolík, O., Stenberg, G., André, M., Owen, C. J., Canu, P., & Dunlop, M. (2007). Source of whistler emissions at the dayside magnetopause. *Geophysical Research Letters*, *34*, L09106. https://doi.org/10.1029/2006GL029195

Webster, J. M., Burch, J. L., Reiff, P. H., Graham, D. B., Torbert, R. B., Ergun, R. E., … Wilder, F. (2017). Magnetospheric Multiscale dayside reconnection electron diffusion region events. http://arxiv.org/abs/1712.09866

Wilder, F. D., Ergun, R. E., Newman, D. L., Goodrich, K. A., Trattner, K. J., Goldman, M. V., … Lindqvist, P. A. (2017). The nonlinear behavior of whistler waves at the reconnecting dayside magnetopause as observed by the Magnetospheric multiscale mission: A case study. *Journal of Geophysical Research: Space Physics*, *122*, 5487–5501. https://doi.org/10.1002/2017JA024062